Whole-Body Averaged Absorbed Power in Insects Exposed to Far-Field Radio Frequency Electromagnetic Fields

Hanne Herssens, David Toribio, Eline De Borre and Arno Thielens

***Abstract*— Insects are exposed to environmental radio frequency electromagnetic fields (RF-EMFs), which are partially absorbed by their body. This absorption is currently unknown for most insect types. Therefore, numerical simulations were performed to study the far-field absorption of RF-EMFs by different insect types at the frequencies between 2 and 120 GHz, which are (expected to be) used in (future) wireless communication. The simulations were done using anatomically accurate as well as spheroid models of the insects. The maximum absorbed power, which ranged from 7.55 to 389 nW for an incident electric field strength of 1 V/m for the studied insect types, was obtained at wavelengths comparable to the insects' size. We created a log-linear model that can estimate absorbed power in insects with an average relative error of <43% between 6 and 120 GHz using only the insects' volume and the frequency as an input using the simulation results. In addition, our simulations showed a very high correlation ($r > 0.95$) between the absorbed power predicted with anatomically accurate insect models and those predicted with spheroid models at the frequencies between 6 and 24 GHz. This suggests that such models could be used to evaluate the RF-EMF exposure of insects in future studies.**

***Index Terms*— Exposure, insects, radio frequency electromagnetic fields (RF-EMFs).**

I. Introduction

WIRELESS communication has become an integral part of everyday life. The technologies used for this communication make use of radio frequency electromagnetic fields (RF-EMFs). Currently, these technologies operate at the frequencies below 6 GHz [1], but they are expected to partly shift to higher frequencies in the future [2], [3]. These RF-EMFs can be absorbed by dielectric objects, such as insects, and can lead to dielectric heating inside these organisms [4], [5]. In the case of insects, this dielectric heating may result in morphological abnormalities [6], abnormal development [7], a change in the reproductive capacity [8], and behavior [9].

This work was supported by the Ghent University Special Research Fund (BOF-UGent) for the Centre of Expertise [Centre for X-ray Tomography of Ghent University (UGCT)] under Grant BOF.EXP.2017.0007. The work of Arno Thielens was supported by the Research Foundation—Flanders (FWO), Brussels, Belgium, under Grant 1283921N. *(Corresponding author: Arno Thielens.)*

The authors are with the Department of Information Technology, Ghent University–imec, 9000 Ghent, Belgium (e-mail: hanne.herssens@ugent.be; david.toribio@ugent.be; eline.deborre@ugent.be; arno.thielens@ugent.be).

Therefore, previous studies have tried to quantify RF-EMF absorption in insects. Liu *et al.* [10] were the first to estimate RF absorption in *Tenebrio molitor* beetles by modeling them as a lossy, dielectric slab. In [11], this was taken one step further, and pupae of the same insect were modeled as prolate spheroids. In more recent publications [12], [13], [14], numerical simulations were used to study the absorption of RF-EMFs in different insect types that are modeled using micro-computerized tomography (micro-CT) scanning. From these studies, it can be concluded that the RF-EMF absorption in insects depends on the frequency of the EMFs, the size of the insects, and the morphology of the insects. In general, it is found that the RF-EMF absorption in insects is maximized at wavelengths that are comparable in size to the insects' dimensions. The shift to higher frequencies for future technologies, and smaller wavelengths, may, thus, induce a change in the absorption of RF-EMFs in insects [12], [13], [14].

While the scanning techniques with micrometer precision used in [12], [13], and [14] are very good to create anatomically accurate models, they are costly and require dedicated scanning equipment and staff trained in operating such equipment and analyzing these scans [14]. Therefore, this approach is not feasible when studying larger sets of insects and RF-EMF exposure scenarios. The same problem was also encountered in the modeling of RF-EMF exposure of vertebrates and humans, which led to the use of prolate spheroids as proxies [15], [16]. These models can be easily created in a computer aided design software and can be used to reduce the number of simulations when analyzing a range of exposure scenarios, due to the symmetries of a spheroid [16]. A disadvantage is that the model does not represent an organism's morphology accurately, so while the whole-body averaged absorbed power might be estimated correctly, it does not provide any information on the actual distribution of the EMFs inside the studied organisms. In [15], it is seen that a spheroid leads to realistic estimations of the absorbed power in humans. Hence, it is worthwhile investigating whether such spheroid models could also be used to estimate absorbed RF power within insects.

Therefore, the goal of this work was to investigate the frequency and size dependences of the whole-body absorbed power for different insect types using two types of models, i.e., anatomical models and spheroid models. To this aim, we have executed numerical simulations using a set of insect

 https://doi.org/10.1109/TAP.2022.3209201

models, which we have combined with preexisting simulations to create frequency-specific log-linear models that link insect volume and whole-body absorbed power. The same mathematical models were also created based on simulations using spheroid models for insects. Both mathematical modeling approaches were then compared. This study is important to estimate potential effects of RF-EMF exposure on wildlife and for future compliance studies of RF-EMF emitting antennas, which might require evaluation of absorption in wildlife that can approach such antennas, such as flying insects [17].

II. Materials and Methods

A. Insect Types

The absorption of RF-EMFs in insects was investigated in this work using numerical simulations. Two types of models were used in this work: anatomically accurate insect models and spheroid models.

1) Anatomically Accurate Insect Models: The absorption of five insects was determined using numerical simulations. These insects and their dimensions are listed in Table I. The models were obtained from [18], where a shape from silhouette (SFS) method was used to obtain models of four insects: the Black Field Cricket, the Granary Weevil, the Sand Wasp, and the Longhorn Beetle (see Fig. 1). In the SFS method, the images of the sample are taken under different viewing angles. The SFS projects the silhouette of the object into a virtual volume for each viewing angle. The volume outside the silhouette is then carved away, and a 3-D visual hull of the insect is obtained. A disadvantage of this technique is that the concave surfaces are not detected. The 3-D models also need to be calibrated by scaled markers included in the images. The Black Field Cricket, the Sand Wasp, and the Longhorn Beetle models were reconstructed from 144 images of 18 megapixels (MP) each. The Granary Weevil required more images due to its small size, i.e., 4464 images of 18 MP each and 31 multifocus images for the 144 views.

We also developed a model of the Asian Hornet at Ghent University. The hornet came from a repository maintained by the Vespa-Watch project (https://vespawatch.be/). This is a citizen science project that aims to monitor the invasion of the Asian Hornet in Flanders. Within the context of this project, Asian Hornets were caught in Flanders and frozen for research purposes. We used one of these frozen samples to obtain a 3-D model using micro-CT scanning. The hornet was scanned with a voxel size of 0.013 mm at the HECTOR scanner of the Centre for X-ray Tomography of Ghent University (UGCT) [19]. The cooling stage described in [20] was used at a set point of -20 °C to keep the sample in frozen conditions during the data acquisition. The 3-D model of the Asian Hornet was then created using the software VGStudio MAX (Volume Graphics, Heidelberg, Germany), following the methods outlined in [14]. Fig. 1 shows the five models.

2) Spheroid Models: The insect models were also approximated by spheroids, as illustrated in Fig. 2. The dimensions of the spheroid models follow the same methods as used in [15]. The spheroid models are constructed using the dimensions of these insect models listed in Table I. The semi-major axis of the spheroid a is set equal to half the length $2a = L$ of the insect. Note that we quantified the length L as the total model length along the main axis of the insects' thorax. This dimension is the largest dimension of most insect models. However, for some insects, the width (W) is larger than L, because their extremities, such as antennae, wings, and legs, might extend

TABLE I

Names and Dimensions of the Newly Used Insect Models. L, W, and H Are the Outer Dimensions Measured Along the x-, z-, and y-Axes, Respectively. $D = \sqrt{L^2 + W^2 + H^2}$ Is the Diagonal of the Box With Dimensions L, W, and H

Insect	L (mm)	W (mm)	H (mm)	D (mm)	Vol (mm³)
Black Field Cricket (*Teleogryllus oceanicus*)	45.02	22.94	14.54	52.58	1083
Granary Weevil (*Sitophilus granarius*)	4.57	2.14	2.23	5.51	3.224
Sand Wasp (*Bembix sp.*)	19.93	15.13	7.92	26.25	241.1
Longhorn Beetle (*Aridaeus thoracicus*)	23.35	23.38	13.99	35.89	338.7
Asian Hornet (*Vespa velutina*)	23.30	10.79	12.82	28.70	421.7

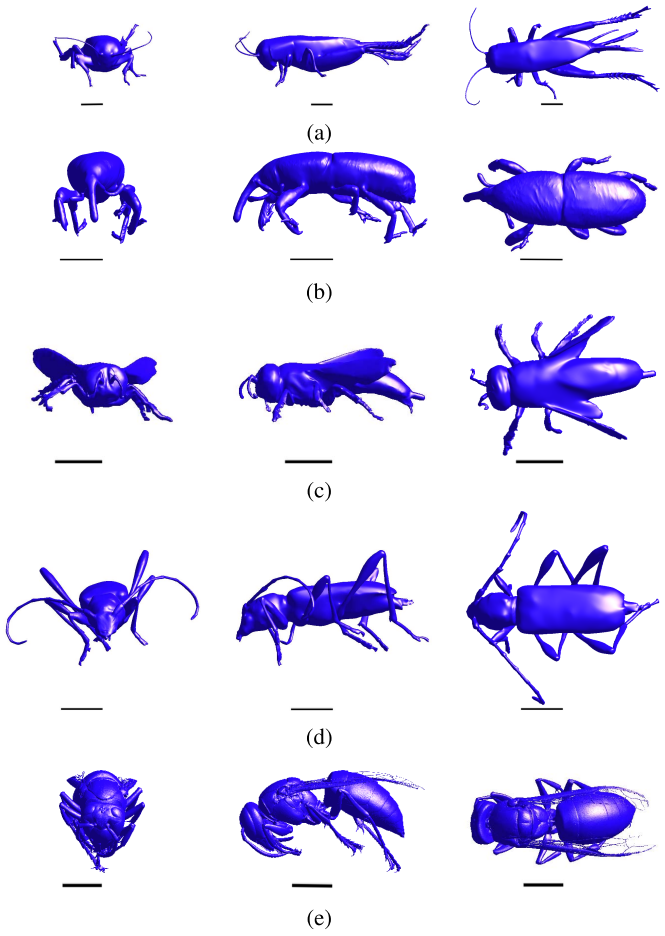

Fig. 1. From left to right: front, side, and top views of the used insect models. The black lines are added as a reference scale. (a) Black Field Cricket with a reference scale of 5 mm. (b) Granary Weevil with a reference scale of 1 mm. (c) Sand Wasp with a reference scale of 5 mm. (d) Longhorn beetle with a reference scale of 5 mm. (e) Asian Hornet with a reference scale of 5 mm.

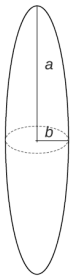

Fig. 2. Spheroid model with semi-major axis a and semi-minor axis b.

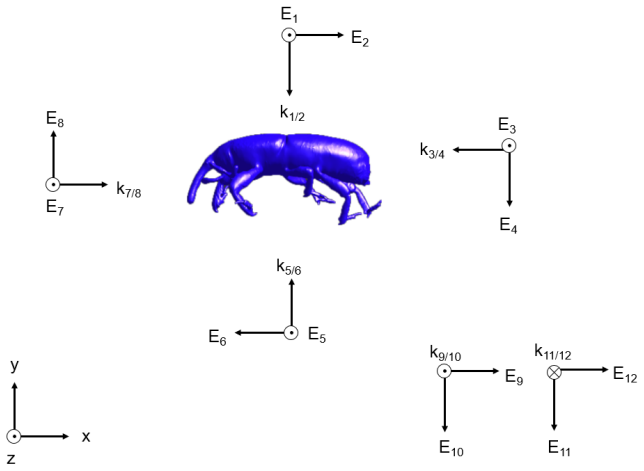

Fig. 3. Twelve single-plane waves that were used for the exposure of the insects. Here, k_i is the wave vector, and E_i is the incident electric field polarization, with $i = 1, \ldots, 12$.

further into space. The semi-minor axis b is calculated from the volume V of the insect: $V = (4/3)\pi ab^2$ [15]. A spheroid has a symmetry plane (xy plane) and a symmetry axis (z-axis, see Fig. 2). This symmetry can be used to reduce the number of simulations that have to be performed. Obviously, a spheroid model will not represent the insect's morphology as accurately as an insect model that is obtained by scanning the insect.

B. Numerical Simulations

The numerical simulations were performed using the finite-difference time-domain (FDTD) method, where Maxwell's equations are discretized. This was done using the commercial software package Sim4Life (Zurich Med Tech, Switzerland). To model far-field RF-EMF exposure, we assumed that the Fraunhofer far-field limit applied to all exposure situations; hence, the exposure can be modeled as plane waves [15].

Far-field exposure was modeled by exposing the insects to incident plane waves for each of the six directions along the insect's three major axes. Since each plane wave has two orthogonal polarizations, this results in 12 incident plane waves (see Fig. 3). The same method was used in [12], [13], and [14] to study the dependence of the absorption on the frequency in insects. For the spheroid models, this reduces to three plane waves due to its symmetry—a plane wave with the wave vector **k** along the major axis of the spheroid (k-polarization), a plane wave with the electric field polarization **E** along the major axis (E-polarization), and a plane wave with the magnetic field polarization **H** along the major axis (H-polarization). The anatomical models of the Black Field Cricket and Granary Weevil were simulated with plane waves at the harmonic frequencies of 2, 3, 6, 12, 24, 60, and 120 GHz with an incoming electric field strength of 1 V/m. The anatomical model of the Longhorn Beetle was only simulated at 6, 12, 24, and 60 GHz, while the anatomical models of the Sand Wasp and the Hornet were only simulated at 6, 12, and 24 GHz. The simulations with the spheroid models were performed at all the frequencies listed above from 2 to 120 GHz, as well as at 90 GHz.

TABLE II
INSECT DIELECTRIC PROPERTIES AT DIFFERENT FREQUENCIES

f (GHz)	2	3	6	12	24	60	90	120
ϵ_r (.)	39.9	38.8	38.0	26.0	14.9	7.02	5.88	5.46
σ (S/m)	1.35	2.05	5.05	11.5	21.1	27.9	28.86	29.2

TABLE III
SIMULATED PERIODS FOR THE DIFFERENT INSECT TYPES

f (GHz)	2	3	6	12	24	60	90	120
Black Field Cricket								
T_{min}	9	10	12	12	14	15	-	18
T_{max}	14	14	15	14	19	30	-	40
T_{avg}	11	12	13	13	16	22	-	32
Granary Weevil	20	20	20	20	30	30	-	30
Longhorn Beetle	-	-	20	30	30	30	-	-
Sand Wasp	-	-	20	30	30	-	-	-
Hornet	-	-	15	20	20	-	-	-
Spheroid models	10	15	15	20	30	40	40	40

The frequency-dependent dielectric properties, the relative permittivity (ϵ_r), and the conductivity [σ (S/m)] assigned to the different models were obtained from [12]. The magnetic properties of the insects were assumed to be the same as air. All insects were modeled as homogeneous objects, i.e., we assumed that they consist out of a single material, which is an approximation of reality. In addition, we used the same, averaged (see [12]) dielectric properties for all insects, because no species-specific properties exist for the studied species. Table II lists the used the same dielectric properties in this study.

The FDTD algorithm divides space in small cubes using a rectilinear grid. The grid step was chosen, such that there are at least ten steps per wavelength ($\lambda/\sqrt{\epsilon_r}$). The maximum grid step used was 0.1 mm. In case of the anatomical model of the Granary Weevil, a smaller maximal grid step of 0.05 mm was chosen to preserve its anatomical features. The spheroid models of the Black Field Cricket and the Granary Weevil were modeled with a maximal grid step of 0.1 and 0.025 mm, respectively. All other spheroid models were modeled with a maximal grid step of 0.05 mm. The simulation domain was bounded by uniaxial perfectly matched layers (UPMLs).

The simulation time was chosen, such that all plane wave simulations reach a steady-state solution of the electric field distribution. This was done by monitoring the electric field

along a line in the simulation domain. The required number of periods was between 9 and 40, depending on the used frequency and insect type. Table III lists the exact values for each model at the simulated frequencies. For the Black Field Cricket anatomical model, the simulations corresponding with the plane waves considered in Fig. 3 did not use a fixed number of periods. Therefore, the average (T_{avg}), minimum (T_{min}), and maximum (T_{max}) number of simulation periods are given.

The harmonic FDTD simulations will result in a steady-state electric field distribution in the simulation domain. From these electric fields, the whole-body averaged absorbed power (P_{abs}) can be calculated. The absorbed power can be used as a proxy for the dielectric heating [4]. The absorbed power is determined as follows:

$$P_{abs} = \int_V \sigma E_{rms,int}^2 dV \tag{1}$$

with $E_{rms,int}$ the root mean-squared (rms) internal electric field, σ the conductivity, and V the total volume of the insect.

Numerical simulations will have some uncertainties associated with them. The simulations were performed with a certain grid step and for a certain simulation time. To investigate if these choices were good, additional simulations with the Granary Weevil were run at 120 GHz for plane wave no. 3 with a smaller grid step (half of the initially chosen step) and for a larger simulation time (double of the initially chosen time). While one setting was investigated, all other simulation parameters were kept constant. The obtained P_{abs} was compared with the original value obtained using the settings described in the previous paragraphs.

The value of the dielectric properties comes with their own uncertainties (see [12]), and these will also influence P_{abs}. Therefore, simulations were performed with different values for these dielectric properties: we executed simulations with the Granary Weevil model and incident plane wave with configuration no. 3 at 2 GHz, for [0.5 $Re(\epsilon_r)$, 0.5 $Im(\epsilon_r)$], [0.5 $Re(\epsilon_r)$, 1.5 $Im(\epsilon_r)$], [1.5 $Re(\epsilon_r)$, 0.5 $Im(\epsilon_r)$], and [1.5 $Re(\epsilon_r)$, 1.5 $Im(\epsilon_r)$], with $Re(\epsilon_r)$ and $\sigma(Im(\epsilon_r)\infty)$ given in Table II, to examine how a $\pm 50\%$ uncertainty influences P_{abs}.

It is uncertain that the 12 chosen plane waves will accurately quantify the exposure of the insect. Therefore, 15 additional simulations were performed for the Longhorn Beetle at a frequency of 24 GHz where the angles of incidence of the plane waves were assigned random values obtained from a uniform distribution. These additional simulations were performed for both the anatomical and spheroid models of the beetle.

C. Analysis of Simulation Results

In the analysis of the EMF absorption by insects, not only the results obtained for the insect types mentioned above were used, but also the results from the preexisting simulations studies. We obtained $P_{abs}(f)$ for a Desert Locust (*Schistocerca gregaria*) with a volume of 1859 mm^3, an Australian Stingless Bee (*Tetragonula carbonaria*) with a volume of 6.2 mm^3, a Beetle (*Geotrupes stercorarius*) with a volume of 21 mm^3, and a Honey Bee Worker (*Apis mellifera*) with a volume of 55 mm^3 from [12]. The same quantities were obtained for another Honey Bee Worker with a volume of 162 mm^3, a Honey Bee Larva with a volume of 512 mm^3, a Honey Bee Drone with a volume of 368 mm^3, and a Honey Bee Queen with a volume of 310 mm^3, from [13]. Three female (volumes 1.1–1.4 mm^3) and three male (volumes 0.7–0.9 mm^3) Yellow Fever Mosquitoes (*A. aegypti*) were obtained from [14]. The dielectric properties used to simulate all these insects were the same ones as the ones used in this manuscript, except for the mosquitoes from [14], which were simulated with dielectric properties specifically obtained for mosquitoes.

For these insect types, spheroid models were constructed based on their dimensions (available in the references cited above), as explained in Section II-A2. The maximal grid steps used for the Desert Locust model, the Australian Stingless Bee, and the mosquitoes were 0.1, 0.025, and 0.025 mm, respectively. All other spheroid models were modeled with a maximal grid step of 0.05 mm. The number of simulated periods for these spheroid models was the same as those listed in Table III.

Using the simulation results presented in this manuscript and those obtained from the literature, we investigated the influence of insect volume on $P_{abs}(f)$ both for the anatomical model and the spherical models. To this aim, we calculated the arithmetic average over all angles of incidence and all polarizations $< P_{abs} >$ for each insect model at each frequency. These averages were then pooled per frequency and used as an input of the following linear model:

$$log_{10}\left(\frac{\langle P_{abs}\rangle}{1\ W}\right) = a + b \times log_{10}\left(\frac{V}{1\ \text{mm}^3}\right) + \chi(\mu, std) \tag{2}$$

with $\chi(\mu, std)$ a Gaussian distributed error term with mean (μ) and standard deviation (SD, std). This model was fit to the simulation data at each frequency separately using least-squares regression, leading to the estimations of the parameters a and b with an associated root-mean-squared error (RMSE)

$$RMSE = \sqrt{\frac{\sum_{i=1}^{n}\left(log_{10}\left(\frac{\langle P_{abs,i}\rangle}{1\ W}\right) - log_{10}\left(\frac{\hat{P}_{abs,i}}{1\ W}\right)\right)^2}{n}} \tag{3}$$

with $\hat{P}_{abs,i}$ the estimations of the model of (2), $\langle P_{abs,i}\rangle$ the mean of the simulated values of the absorbed power for insect (i), and n the number of data points (insects) at the considered frequency. The fits obtained for the anatomical models and the spheroid models are then compared with each other. We also determined the absolute relative error ($error_{avg}$, as a percentage) of the $\langle P_{abs}\rangle$ prediction in comparison with the simulated value at each frequency, using the following:

$$error_{avg} = \frac{1}{n}\sum_{i=1}^{n}\frac{100 \cdot \left|\langle P_{abs,i}\rangle - \hat{P}_{abs,i}\right|}{\langle P_{abs,i}\rangle}. \tag{4}$$

A lower $error_{avg}$ indicates a better fit.

Finally, we compared the simulated values for the anatomical models and the spheroid models created for the same insects using two metrics: the absolute relative error and the Pearson correlation between both. The absolute relative error

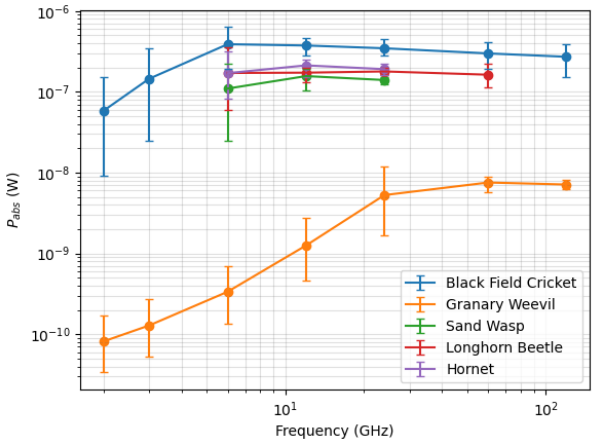

Fig. 4. P_{abs} as a function of frequency for the different anatomical insect models listed in Table I for $E_{inc} = 1$ V/m. The dots represent the mean of P_{abs} over the 12 plane waves. The whiskers indicate the maximum and minimum values obtained at a given frequency.

$error_{avg,sphe}$ is calculated as follows:

$$error_{avg,sphe} = \frac{1}{n}\sum_{i=1}^{n}\frac{100\cdot\left|\langle P_{abs,ana,i}\rangle - \langle P_{abs,sphe,i}\rangle\right|}{\langle P_{abs,ana,i}\rangle} \quad (5)$$

with $\langle P_{abs,ana,i}\rangle$ and $\langle P_{abs,sphe,i}\rangle$ the mean simulated absorbed power for the anatomical and the spheroid models of the same insect (i) at the same frequency, respectively. We also calculated the Pearson correlation coefficient between the same two quantities, because even with relatively large errors on the basis of individual insects, it might be that the values of anatomical and spheroid models are highly correlated, which would indicate the usability of the spheroid models.

III. Results

A. Anatomical Insect Models

Fig. 4 shows the simulated P_{abs} as a function of frequency for different insect types when using anatomical accurate insect models. The curves were determined over the full frequency range for the Granary Weevil and the Black Field Cricket. The curves for both insects show the same frequency behavior, namely, an initial increase, followed by a decrease in the mean P_{abs}. The maximum mean P_{abs} is found at $f \geq$ 6 GHz for all studied insects. Looking at the corresponding wavelengths, it is seen that the maximum P_{abs} is found at a free-space wavelength comparable to the insect's size (see Table I). The same frequency behavior was also found for the insects obtained from the literature [12], [13], [14]. Therefore, the remaining insects were only simulated in the frequency range where the maximal P_{abs} is predicted, based on their dimensions. Fig. 4 shows that the curves indeed show a local maximum in this frequency range. A local maximum was found at 12 GHz for the Sand Wasp and the Hornet and at 24 GHz for the Beetle, respectively.

Fig. 5 shows P_{abs} found for the anatomical insect models simulated in this work and in the literature, as a function of volume at 6, 12, and 24 GHz, alongside a linear fit using the model shown in (2). The fit parameters of the model are listed in Table IV. It can be observed that on a log–log graph, P_{abs} as a function of the insects' volume is approximately linear. It is also seen that the largest variation in P_{abs} for a certain insect is found for a frequency near the peak frequency. For instance, for the Locust (V = 1859 mm^3) and the Black Field Cricket (V = 1083 mm^3), Fig. 5(a) shows that at 6 GHz (the peak frequency for the Locust and the Black Field Cricket), the difference between the minimum P_{abs} and the maximum P_{abs} is greater than the difference at 12 and 24 GHz. This same effect is also visible in Fig. 4 for all simulated insects except for the black field cricket, which shows higher variations below the peak absorption frequency.

TABLE IV

Fit Coefficients a and b With SD for Anatomical Insect Models

	a	b	RMSE
6 GHz	-9.87 ± 0.061	1.16 ± 0.032	0.16
12 GHz	-9.36 ± 0.045	1.02 ± 0.023	0.12
24 GHz	-8.94 ± 0.051	0.85 ± 0.027	0.13

TABLE V

Fit Coefficients a and b With SD for Spheroid Insect Models

Frequency	a	b	RMSE
6 GHz	-10.05 ± 0.075	1.19 ± 0.040	0.2
12 GHz	-9.36 ± 0.050	0.96 ± 0.026	0.13
24 GHz	-8.73 ± 0.028	0.70 ± 0.015	0.07
60 GHz	-8.55 ± 0.016	0.62 ± 0.008	0.04
90 GHz	-8.51 ± 0.016	0.59 ± 0.008	0.04
120 GHZ	-8.46 ± 0.014	0.57 ± 0.007	0.04

In Table IV, it is observed that for a higher frequency, a higher offset (a) is obtained, but a lower slope (b). This suggests that if the frequency keeps rising, the absorbed power will reach a plateau. The RMSE and the average relative errors are higher at 6 GHz in comparison with 12 and 24 GHz, because the angular variation of P_{abs} is higher at this frequency. The relative error of 35% at 6 GHz is still relatively low in comparison with the differences in P_{abs} that can exist between different insects at this frequency (see Fig. 5). It is expected that, for increasing frequency, the linear fit will become more accurate.

B. Spheroid Insect Models

Fig. 6 shows P_{abs} as a function of the volume at a given frequency for the spheroid models. It is seen that the highest variation in P_{abs} for a certain insect is found for a frequency near the peak frequency. This was also the case for the anatomical insect models. The lowest variation is observed for frequencies just above the peak frequency for a certain insect type.

To further analyze the volume behavior of P_{abs}, a fit following (2) is performed for each individual frequency. The values of the fit coefficients are given in Table V together with their SD and the RMSE. When comparing these fits with the ones obtained for the anatomical insect models, a similar behavior is observed. The offset increases, and the slope decreases with increasing frequency. The coefficients for the fits at 6, 12, and 24 GHz for both model types are also similar. The fit coefficients at 6 and 12 GHz obtained with the spheroid

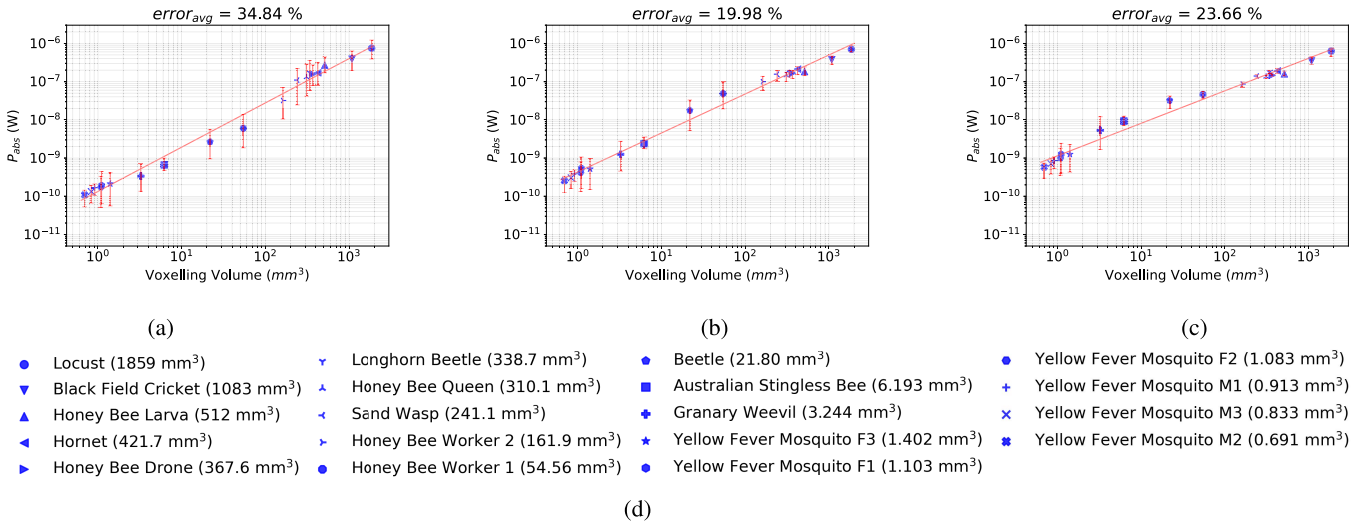

Fig. 5. P_{abs} as a function of the volume for different anatomical insect models at (a) 6, (b) 12, and (c) 24 GHz for $E_{inc} = 1$ V/m. A linear fit is performed on a log–log scale using the means over the 12 incident plane waves. The whiskers indicate the minimum and maximum values obtained by a specific insect model at a given frequency. (d) Legend.

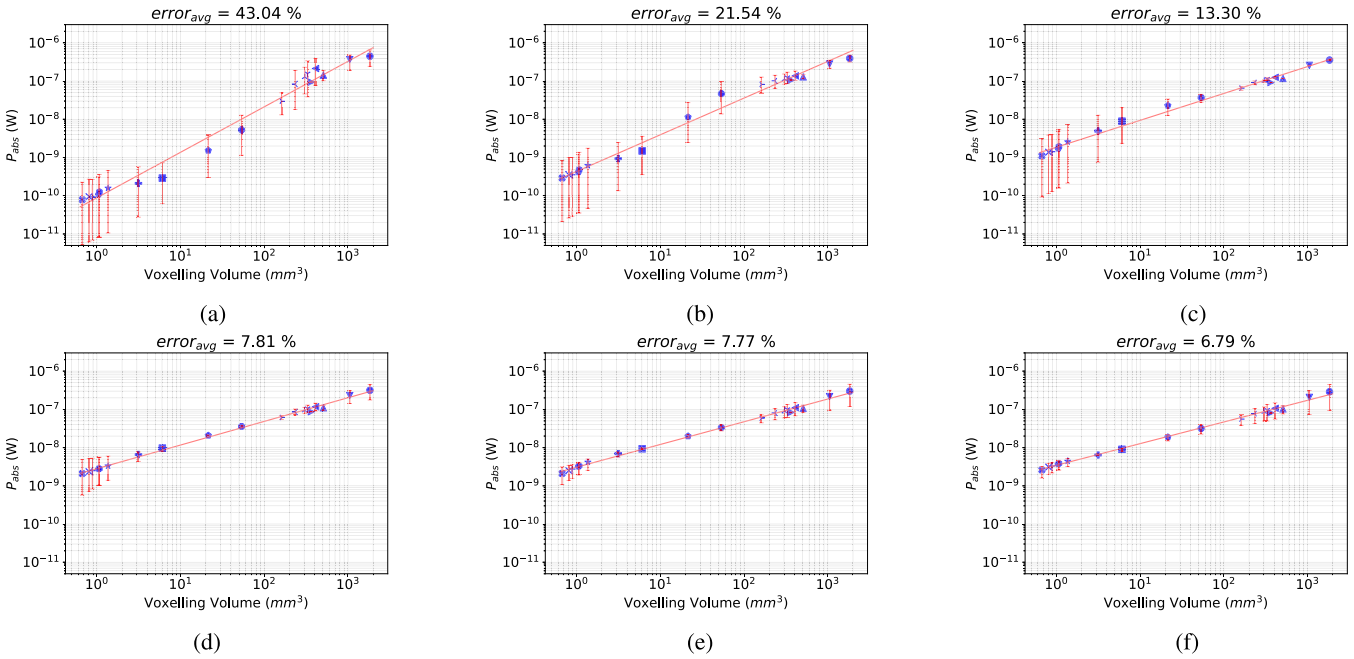

Fig. 6. P_{abs} as a function of the volume for the different spheroid models of the insect types listed in Fig. 5 at (a) 6, (b) 12, (c) 24, (d) 60, (e) 90, and (f) 120 GHz for $E_{inc} = 1$ V/m. A linear fit is performed on a log–log scale using the means over the 12 incident plane waves. The whiskers indicate the minimum and maximum values obtained by a specific insect model at a given frequency.

models lie within the SD of the fit coefficients obtained using the anatomical models. Looking at the average of the absolute relative error given in Fig. 6 and the RMSE given in Table V, it is seen that again the fits at higher frequencies perform better. The highest absolute relative errors at 6 and 12 GHz are obtained for the Australian Stingless Bee. At 24 GHz, the highest errors are obtained for the Beetle, while at 60 and 90 GHz, these are obtained for the Honey Bee Drone. The maximum error at 120 GHz is found for the Honey Bee Drone. Fig. 6 also shows that the fits at 60, 90, and 120 GHz are very similar. This again suggests that, at a given volume, for a higher frequency, P_{abs} will not vary that much compared with the lower frequencies.

C. Comparison of Anatomical and Spheroid Models

To verify if the spheroid models can be used to predict P_{abs} in the far-field for the considered insect types, the results obtained using the spheroid models $P_{abs,sphe}$ were compared with the ones obtained using the anatomical models $P_{abs,ana}$ for all insect types described above. Fig. 7 shows $P_{abs,sphe}$ versus $P_{abs,ana}$ at the frequencies of 6, 12, and 24 GHz. If both results would be perfectly in line with each other, all data points would lie on the bisector. The Pearson correlation coefficient r is also given in the same figure. The correlation coefficients of 0.957, 0.989, and 0.99 with p-values smaller than 0.001 were found at 6, 12, and 24 GHz, respectively.

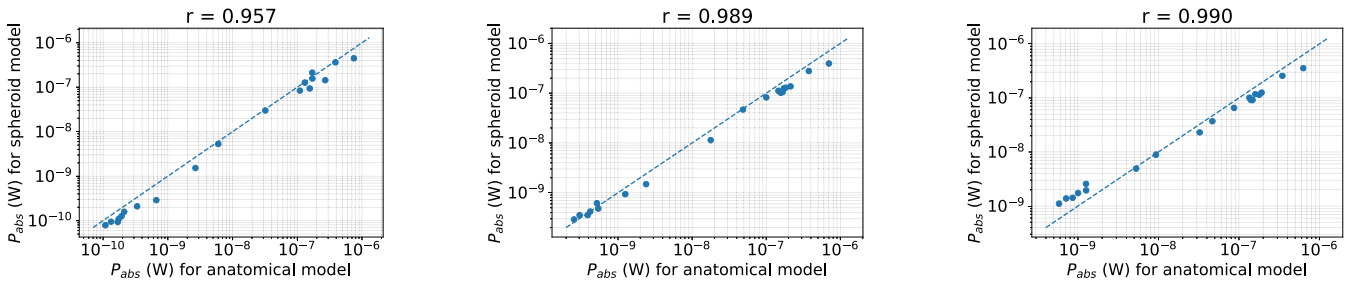

(a) (b) (c)

Fig. 7. Comparison of the obtained P_{abs} for the anatomical and spheroid models of insects at (a) 6, (b) 12, and (c) 24 GHz for $E_{inc} = 1$ V/m. The Pearson correlation coefficient r is also given.

The p-values indicate there is more than 99.9% ($p < 0.001$) certainty that there is correlation present between the results obtained using the spheroid models and the results obtained using the insect models.

We also investigated the relative errors between $P_{abs,spheroid}$ and $P_{abs,insect}$, relative to the former and found mean errors of 29%, 24%, and 44%, at 6, 12, and 24 GHz, respectively. The highest errors were found for the mosquitoes, for which a mosquito-specific set of dielectric parameters were used. These are also the smallest studied insects and are furthest away from resonance at 6–24 GHz.

D. Simulation Uncertainties

The influence of four settings, i.e., the grid step, the simulation time, the dielectric properties, and the angles of incidence, on P_{abs} was investigated for both the anatomical insect models and the spheroid models. The influence of the grid step on P_{abs} is the highest at the smallest simulated wavelength, i.e., at 120 GHz. For the anatomical Granary Weevil model and incident plane wave with configuration no. 3 in Fig. 3, the grid step was set to 0.025 mm instead of 0.05 mm. Reducing the grid step resulted in a relative error of 0.84% on P_{abs}. Hence, it can be concluded that the grid step was chosen small enough. Extending the simulation time from 30 periods to 60 periods for the same model, configuration and frequency gave a relative error of 0.003% on P_{abs}. Again, the highest relative error was expected at the highest frequency, since a longer simulation time in terms of simulated periods is expected at higher frequencies and a fixed simulation volume. The exposure of the anatomical models was determined using plane waves incident from six directions, each with two orthogonal polarizations. To verify this choice, additional simulations were run for the Longhorn Beetle at a frequency of 24 GHz, with random angles of incidence taken from uniform distributions for the elevation and azimuth angles over their full extent. The 15 simulations were executed using these distributions. A mean relative error of 3.13% on P_{abs} is obtained. Hence, the 12 plane wave setups seem a good choice for studying far-field exposure. We also varied the dielectric properties of the plane wave simulation with configuration no. 3 for the anatomical Granary Weevil model at 2 GHz and found the relative errors of -2%, 136%, -64%, and 6% on P_{abs} for piecewise adaptations of 50% of ϵ_r and σ, respectively. It is clear that different dielectric properties potentially lead to significantly different results, but these deviations are still smaller than the difference in P_{abs} that is observed for different angles of incidence. For example, the P_{abs} values for configuration 1 and configuration 12 differ by a factor of 5 for the Granary Weevil at 2 GHz.

We also determined the simulation uncertainties for the spheroid models. Reducing the grid step for the spheroid model of the Granary Weevil from 0.025 to 0.0125 mm for an incident plane wave with k-polarization led to a relative error of 0.86%. Doubling the number of simulated periods in the same configuration led to a relative error smaller than $2 \times 10^{-4}\%$. Three plane waves were used for determining the exposure of the spheroid models. To examine whether this gave a good estimation, ten additional simulations were run with random angles of incidence using the spheroid model of the Longhorn Beetle at 24 GHz. A mean relative error of 1.26% on P_{abs} was found. The relative errors of 83%, 246%, -75%, and -29% on P_{abs} were found for piecewise adaptations of 50% of ϵ_r and σ, respectively, for the spheroid model of the Granary Weevil exposed to a plane wave with k-polarization at 2 GHz. While these errors might seem large, they are still relatively small in comparison with the variations up to a factor of 22 obtained for the same insect as a function of the angle of incidence.

IV. Discussion

Fig. 4 shows the simulated P_{abs} as a function of frequency for different insect types. These curves all show a similar dependency on frequency: an increase up to a certain maximum and then a slight decrease as a function of frequency at higher frequencies, with smaller angular dependencies. These results are in line with [12] and [13], where a similar frequency dependence of P_{abs} was found for other insects.

As Figs. 5 and 6 demonstrate, we found a linear relationship between the logarithms of P_{abs} and the insect volume V. While these dependencies were not explicitly determined for vertebrate models in [15], a clear dependency of whole-body averaged SAR on whole-body mass was also found in [15], which is in line with the dependency we found of P_{abs} on volume. In [21] and [22], this dependency of whole-body averaged power on vertebrate animal size is explained by demonstrating that a vertebrate's total surface area increases by the 0.67 power with increasing whole-body mass. A higher

surface area implies a higher effective area that can be exposed to incident RF-EMFs and this higher absorption.

Prior inter-species comparison of RF-EMF exposure is presented in [22] and [23]. Gordon *et al.* [23] presented a comparison of RF-EMF exposure of vertebrates, where they investigated thresholds for thermal effects in different rodents and found a linear dependency between the logarithm of the whole-body averaged SAR and the logarithm of the body mass, with lower whole-body masses requiring a higher whole-body averaged SAR to induce thermal effects. In [22], these values are then used to calculate thresholds for thermal effects in terms of heat flux densities (in W/m^2), based on the estimations of animals' surface areas, not using RF-EMF dosimetry. The results of our study could aid in defining similar thresholds for insects. Our results suggest that the whole-body averaged SAR in insects will decrease with increasing volume (factor $b < 1$) at frequencies > 12 GHz, assuming that the mass and volume in insects scale linearly.

As Fig. 7 demonstrates, we found very high correlations between P_{abs} as determined by the anatomical models and the spheroid models. At the two lowest frequencies, 6 and 12 GHz, we found that the anatomical models more often lead to higher mean P_{abs} values (most markers below the bisector). We explain this effect by a higher chance of probability of the occurrence of local maxima in internal E-fields in the anatomical models, which have more geometrical extremes in comparison with the spheroids (see, for example, the antennae of the Longhorn Beetle).

In general, we found that the simulation settings can have an influence on the results. However, the relative errors that we observed by changing the simulation settings are all relatively small to the variations that can occur in P_{abs} as a function of insect volume and angle of incidence at a fixed frequency. Therefore, we conclude that these errors will not fundamentally alter our observations.

A limitation of our study is the use of insect models with homogeneous dielectric properties. Real insects consist of a variety of tissues, and their dielectric properties will be distributed homogeneously over their body. Prior studies on humans have established that the homogeneous spheroid models can underestimate the whole-body averaged specific absorption rate in children [24] under far-field exposure, and that the variation as a function of the exposure conditions is also underestimated using homogeneous models [24]. Heterogeneous insect models should be used in future studies to validate whether this is also the case for insects. However, such models, nor the tissue-specific dielectric properties necessary to assign to these models, do not exist at this point. These models would also be necessary to quantify partial-body or tissue-specific exposure of insects.

V. Conclusion

Numerical simulations were performed to investigate the absorption of RF-EMFs by different insect types using the anatomical models and the spheroid insect models. Single plane wave exposure was considered to gain insight into the dependence of the absorbed power on the frequency of the RF-EMFs and on the volume of the insect types. The maximum absorbed power, which ranged from $7.55\ 10^{-9}$ to $3.89\ 10^{-7}$ W for $E_{inc} = 1$ V/m, was obtained at wavelengths comparable to the insect's size. For all studied insect types, this was at $f \geq 6$ GHz, which are the frequencies expected to be used in future wireless communication. It was observed that the logarithm of the absorbed power scales linearly as a function of the logarithm of the insect volume. A linear fit using these two quantities had the average errors of less than 35% when the insect models were used and less than 43% when the spheroid models were used. These errors are relatively small in comparison with the variations of more than a factor of 1000 that exist in P_{abs} as a function of insects' volume. This implies that the future estimations of P_{abs} in insects do not necessarily require numerical modeling, but can be done solely on the measurement of insect volume and the use of the mathematical models developed in this study. The P_{abs} values obtained using the anatomical models were compared with the results obtained using the spheroid models, and a high correlation (e.g., $r = 0.957$ and $p < 0.001$ at 6 GHz) between the two sets was found. This shows that in terms of far-field RF-EMF exposure, spheroids can be used to model P_{abs} in insects, which is an important result, because spheroid models are relatively easy to create and lead to drastic reductions in the number of far-field simulations due to symmetry planes in these models. In a future study, we want to investigate whether the thresholds for thermal effects in insects also follow the same trend as found in [23]. A combination of such a study and the results presented here could then derive thresholds for thermal effects in insects in terms of incident power densities or field strengths.

Acknowledgment

The authors would like to thank Karel Schoonvaere of Vespa-Watch to provide the frozen hornet. They would also like to thank Matthieu Boone and Iván Josipovic for scanning the Asian Hornet.

References

[1] M. Velghe, W. Joseph, S. Debouvere, R. Aminzadeh, L. Martens, and A. Thielens, "Characterisation of spatial and temporal variability of RF-EMF exposure levels in urban environments in Flanders, Belgium," *Environ. Res.*, vol. 175, pp. 351–366, Aug. 2019.

[2] D. Colombi, B. Thors, and C. Törnevik, "Implications of EMF exposure limits on output power levels for 5G devices above 6 GHz," *IEEE Antennas Wireless Propag. Lett.*, vol. 14, pp. 1247–1249, 2015.

[3] Z. Pi and F. Khan, "An introduction to millimeter-wave mobile broadband systems," *IEEE Commun. Mag.*, vol. 49, no. 6, pp. 101–107, Jun. 2011.

[4] G. Ziegelberger *et al.*, "Guidelines for limiting exposure to electromagnetic fields (100 kHz to 300 GHz)," *Health Phys.*, vol. 118, no. 5, pp. 483–524, May 2020.

[5] S. O. Nelson, P. G. Bartley, and K. C. Lawrence, "RF and microwave dielectric properties of stored-grain insects and their implications for potential insect control," *Trans. ASAE*, vol. 41, no. 3, pp. 685–692, 1998.

[6] A. M. Kadoum, H. J. Ball, and S. O. Nelson, "Morphological abnormalities resulting from radiofrequency treatment of larvae of tenebrio molitor1," *Ann. Entomol. Soc. Amer.*, vol. 60, no. 5, pp. 889–903, Sep. 1967.

[7] R. L. Carpenter and E. M. Livstone, "Evidence for nonthermal effects of microwave radiation: Abnormal development of irradiated insect pupae," *IEEE Trans. Microw. Theory Techn.*, vol. MTT-19, no. 2, pp. 173–178, Feb. 1971.

[8] T. L. Pay, F. A. Andersen, and G. L. Jessup, "A comparative study of the effects of microwave radiation and conventional heating on the reproductive capacity of Drosophila melanogaster," *Radiat. Res.*, vol. 76, no. 2, pp. 271–282, 1978.

[9] W. Harst, J. Kuhn, and H. Stever, "Can electromagnetic exposure cause a change in behaviour? Studying possible non-thermal influences on honey bees—An approach within the framework of educational informatics," *Acta Systemica, IIAS Int. J.*, vol. 6, no. 1, pp. 1–6, 2006.

[10] L. Liu, F. Rosenbaum, and W. Pickard, "Electric-field distribution along finite length lossy dielectric slabs in waveguide," *IEEE Trans. Microw. Theory Techn.*, vol. MTT-24, no. 4, pp. 216–219, Apr. 1976.

[11] O. Fujiwara and Y. Amemiya, "Microwave power absorption in a biological specimen inside a standing-wave irradiation waveguide," *IEEE Trans. Microw. Theory Techn.*, vol. MTT-30, no. 11, pp. 2008–2012, Nov. 1982.

[12] A. Thielens, D. Bell, D. B. Mortimore, M. K. Greco, L. Martens, and W. Joseph, "Exposure of insects to radio-frequency electromagnetic fields from 2 to 120 GHz," *Sci. Rep.*, vol. 8, no. 1, pp. 1–10, Dec. 2018.

[13] A. Thielens, M. K. Greco, L. Verloock, L. Martens, and W. Joseph, "Radio-frequency electromagnetic field exposure of western honey bees," *Sci. Rep.*, vol. 10, no. 1, pp. 1–14, Dec. 2020.

[14] E. De Borre *et al.*, "Radio-frequency exposure of the yellow fever mosquito (A. Aegypti) from 2 to 240 GHz," *PLOS Comput. Biol.*, vol. 17, no. 10, Oct. 2021, Art. no. e1009460.

[15] C. H. Durney, H. Massoudi, and M. F. Iskander, "Radiofrequency radiation dosimetry handbook," Dept. Elect. Eng., Utah Univ., Salt Lake City, UT, USA, Tech. Rep. ADA180678, 1986.

[16] G. Vermeeren, W. Joseph, C. Olivier, and L. Martens, "Statistical multipath exposure of a human in a realistic electromagnetic environment," *Health Phys.*, vol. 94, no. 4, pp. 345–354, 2008.

[17] D. Toribio, W. Joseph, and A. Thielens, "Near field radio frequency electromagnetic field exposure of a western honey bee," *IEEE Trans. Antennas Propag.*, vol. 70, no. 2, pp. 1320–1327, Feb. 2021.

[18] C. V. Nguyen, D. R. Lovell, M. Adcock, and J. La Salle, "Capturing natural-colour 3D models of insects for species discovery and diagnostics," *PLoS ONE*, vol. 9, no. 4, Apr. 2014, Art. no. e94346, doi: 10.1371/journal.pone.0094346.

[19] B. Masschaele *et al.*, "HECTOR: A 240 kV micro-CT setup optimized for research," *J. Phys., Conf.*, vol. 463, Oct. 2013, Art. no. 012012.

[20] T. De Schryver *et al.*, "A compact low cost cooling stage for lab based X-ray micro-CT setups," in *Proc. AIP Conf.*, Jan. 2016, Art. no. 020018.

[21] C. J. Gordon and J. H. Ferguson, "Scaling the physiological effects of exposure to radiofrequency electromagnetic radiation: Consequences of body size," *Int. J. Radiat. Biol. Rel. Stud. Phys., Chem. Med.*, vol. 46, no. 4, pp. 387–397, Jan. 1984.

[22] C. J. Gordon, "Normalizing the thermal effects of radiofrequency radiation: Body mass versus total body surface area," *Bioelectromagnetics*, vol. 8, no. 2, pp. 111–118, 1987.

[23] C. J. Gordon, M. D. Long, K. S. Fehlner, and A. G. Stead, "Body temperature in the mouse, hamster, and rat exposed to radiofrequency radiation: An interspecies comparison," *J. Thermal Biol.*, vol. 11, no. 1, pp. 59–65, Jun. 1986.

[24] G. Vermeeren, W. Joseph, and L. Martens, "Statistical multi-path exposure method for assessing the whole-body SAR in a heterogeneous human body model in a realistic environment," *Bioelectromagnetics*, vol. 34, no. 3, pp. 240–251, 2013.